DOI: 10.13009/EUCASS2019-140

DOI: ADD DOINUMBER HERE

Numerical study of side loads generation in over-expanded conical nozzles

Boubakr ZEBIRI⋆, Arthur PIQUET and Abdellah HADJADJ
CORIA INSA de Rouen & Université de Rouen, 76000 Rouen, France
boubakr.zebiri@insa-rouen.fr · arthur.piquet@intradef.gouv.fr · abdellah.hadjadj@insa-rouen.fr
⋆Corresponding author

Abstract

The flow pattern in over-expanded conical nozzles is numerically investigated by means of three-dimensional wall-modeled large-eddy simulations (WM-LES). The objective of the study is to identify the origin of the low-frequency oscillations (LFO) and the side-loads generation observed in separated supersonic flows. The computational results are compared with the available experimental data for validation. The simulations bring clear evidence of the existence of broadband and energetically-significant LFO in the vicinity of the separated shock. The magnitude of the shock excursions was less important in the conical case, compared to the planar nozzle, because of the strong adverse pressure gradient that develops upstream of the separation zone. The generated side-loads were analyzed and a dynamic mode decomposition (DMD) analysis reveals the existence of two types of modes: the non-helical modes which are low-frequency modes based mainly in the streamwise forces and the helical modes which are high-frequencies modes, compared to the first Type. The laters mainly concern the side-loads.

1. Motivation and background

With the renewed interest in supersonic flights, studying flow inside supersonic nozzles is becoming of such importance especially for rockets, aircrafts and supersonic vehicles. As a matter of fact, during the take-off and the first phase of flight, the ratio between the reservoir (or the combustion chamber) pressure to the atmospheric pressure is significantly lower than the nominal ratio. The nozzle then operates in an over-expanded regime, which has the effect of generating a system of a recompression shock. The later causes the separation of the boundary layer from the wall. The distribution of this separation line is often random, making the flow asymmetrical and promoting the appearance of lateral forces. Besides, the pressure fluctuations in magnitude and direction, induced by this separation, can affect the characteristics of the resulting thrust vector and adversely affect the overall performance of the vehicle. These unsteady phenomena occur at low frequencies which may involve scales that are likely to constitute a source of aerodynamic excitation of certain structural eigenmodes and be detrimental to its integrity. Lateral forces are therefore a limiting factor in the design of nozzle geometries, since they generally result in a choice of thicker (and therefore heavier) or shorter (and therefore less propulsive) nozzles. In such configurations, other sources of instabilities can be identified such as the mixing layer, boundary layer and the recirculation zones, which makes this flow quite complex and challenging to study. In terms of flow separation, two types of configuration can be found: Free Shock Separation (FSS) and Restricted Shock Separation (RSS). The transition between them leads to a sudden change in the wall pressure distribution resulting in strong side-loads.[11,12] When the flow separates inside the nozzle, it creates a system of shock interacting with the separated boundary layer known as shock wave boundary layer interaction (SWBLI). The SWBLI may exhibit strong unsteadiness that affects the symmetry of the flow which can yield dangerous lateral forces.[10] Another principal reason to study nozzle flows is to better understand the occurrence of low-frequency oscillation (LFO) in the vicinity of the separated shock. This phenomenon is associated with complex flow structures, including vortex shedding, jet oscillations and multiple shock reflections, was investigated by many researchers.[3,6,8,14,18,25–27] Two main categories of LFO mechanisms can be broadly found: The first points out the upstream influence of the incoming turbulent boundary layer, while the second concerns the downstream influence via the interaction between the separated boundary layer, the recirculation region, and the shock system. Few hypotheses have been formulated for the first category. For instance, Ganapathisubramani *et al*[9] reported the existence of very long coherent structures of fifty boundary-layer thicknesses long with a correlation between the low-frequency response of the separation point and these large-scale regions of the incoming turbulent boundary layer, these structures are found to scale with $\bar{u}/2\lambda$ where $\bar{u}$ is the upstream

DOI: 10.13009/EUCASS2019-140

freestream velocity and λ is the size of the eddies structure. This scale was confirmed when comparing with the work of Dupont *et al* .[6] Additionally Ünalmis *et al* [1] consider that the LFO can be a result of the thickening and thinning of the upstream boundary layer. This hypothesis was refused later by Beresh *et al* .[2] The later found a correlation between the LFO of the shock and the upstream velocity fluctuations for the same configuration of a compression corner. However, many explanations can be found in the second category. They may defer in the mechanism in which the low-frequency phenomena occur but they are all produced by the downstream conditions. For instance, Piponniau *et al* [19] proposed a model in which they explain the breathing of the separation bubble and the low-frequency shock motion in terms of fluid entrainment in the mixing layer, whereby fluid from the separation bubble is continuously entrained in the mixing layer, sheded downstream and replenished at a time scale corresponding to the low-frequency shock oscillations. Daussage *et al* [8] considered the eddies in the separated region as the main source of excitation of the LFO. Pirrozoli *et al* [22] proposed a scenario in which the LFO may be produced by acoustic disturbance resulting from the interaction of the coherent structures, shed by the mixing layer next to the separation point, and the incident shock. Zaman *et al* [27] investigated experimentally and theoretically shock-wave oscillations in transonic diffusers. They concluded that the mechanism creating LFO is stimulated by acoustic resonance, where the low-frequency mode corresponds to the case when the one-quarter wavelength is fitted within the approximate distance from the foot of the shock to the nozzle exit. The same conclusions were made by Johnson *et al* [14] when investigating, experimentally, the flow in supersonic planar nozzles. Olson *et al* [18] investigated numerically the same nozzle as[14] and confirmed the previous findings. Martelli *et al* [17] found that the self-sustained oscillation is driven by a pressure imbalance between the pressure level downstream the shock and the ambient. Based on the above mentioned remarks, it is clear that supersonic nozzle flow, in particular the associated low-frequency unsteadiness, is still an active field of investigation. Intending to shed some light into this complex physics, three-dimensional high-fidelity large-eddy simulations are used. The current work uses WM-LES to simulate the flow inside an over-expanded conical nozzles. The objective is to study very long time series associated with LFO. Additionally, a dynamic mode decomposition is performed to better understand the behavior of these phenomena.

2. Mathematical and numerical aspects

The code used in this work is a curvilinear explicit finite-differences Navier Stokes solver, written in a generalized coordinates system, with WCNS (Weighted Compact Nonlinear Scheme) /Central hybrid scheme for space discretization and RK4 (4th-order Runge Kutta) for time integration. The code uses the HDF5 library for IO and the MPI library for parallelization. It also uses the wall-model developed in Piquet.[20] Fig. 1-(a) shows the grid representation with the two overlapping grids. The internal grid, Ω_0, and the external grid Ω_1. This choice comes with the centerline-singularity issue and the associated time-step restriction. A possible compromise is to use a domain decomposition method (DD). For this purpose, a custom DD method has been developed. (with more details given in Piquet *et al* [21]). The overlapping limit between the two grid is set to $R_{\Omega_0} = 0.6R(x)$, where $R(x)$ is the outer radius of the cross section at the streamwise position x. The buffer zone between the inlet and the throat is approximately 28 inlet boundary layer thickness δ_i, allowing sufficient extent for the boundary layer to develop. The outside domain is similar to the planar nozzle flow of Piquet[20] with $20H_{th}$ length. For convenience, all figures presented in this paper will use the classical wall-normal notation y, equivalent to the radius coordinates $y = (r - R_{\Omega_0})cos(\theta)$. The angular/spanwise direction θ will be represented by the z-direction, unless otherwise specified.

The characteristics of the incoming boundary layer are similar to the planar case of Piquet[20] and adapted for the cylindrical coordinates r-θ. The Reynolds number (Re) is $Re = u_{i,\infty} R_{th}/\nu_{i,\infty} \simeq 90000$, where $u_{i,\infty}$, $\nu_{i,\infty}$ and R_{th} are the inlet freestream velocity, the kinematic viscosity and the nozzle throat radius, respectively. For the outlet boundary condition, we use a buffer zone combined with pressure far-field boundary conditions to damp the outcoming waves. For better comparison with the planar case, the shock positions have been adjusted for both nozzles. Since reducing the divergent angle to the adequate value leads to a pipe flow (the nozzle area ratio, in this case, (ε) will be 1.2) the NPR is adjusted to 2.0, so that the isentropic profiles between the planar and the cylindrical nozzles are similar.

The numerical data from unsteady LES calculations are averaged over a long dimensionless time of $t^\star \sim 18000$ with $t^\star = t.u_{i,\infty}/\delta_i$.

	N_x	$N_y^{\Omega_0}$	$N_z^{\Omega_0}$	$N_y^{\Omega_1}$	$N_z^{\Omega_1}$	L_b/H_{th}	Δx_i^+	Δy_i^+	$R\ \Delta\theta_i^+$	Nb cells
WM-LES	672	81	81	26	256	2.8	60	45	40	8.8 M

Table 1: Grid parameters of the cylindrical nozzle configuration.

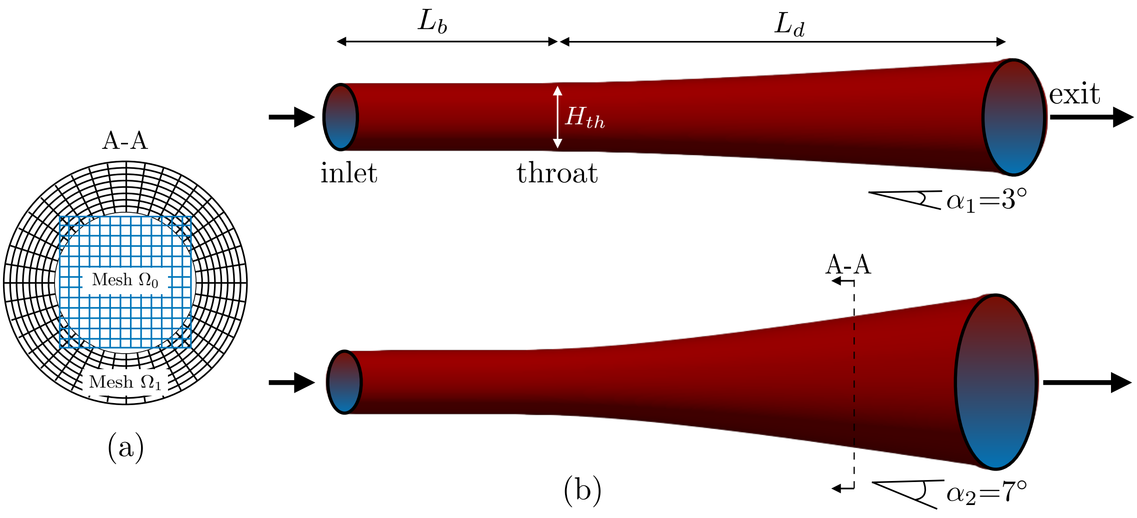

Figure 1: (a) Grid representation; Internal mesh Ω_0 (cartesian coordinates), External mesh Ω_1 (cylindrical coordinates). (b) Schematic representation of the two nozzle configurations with: $\alpha_1 = 3°$, $\alpha_1 = 7°$, $L_b = 2.8\ H_{th}$ and $L_d = 6.6\ H_{th}$, H_{th} being the nozzle throat diameter.

3. Results and discussion

The distribution of the Clauser's parameter $\beta = \frac{\delta^\star}{\tau_w}\frac{dp}{dx}$ along the x-direction is shown in Fig. 2. A good agreement is found between the numerical and the experimental results. One can see that in the divergent section, the pressure gradient is amplified by a factor between 25% to 40% compared to the planar case.

The normalized wall mean and r.m.s pressure profiles are shown in Fig. 3. The p' is slightly reducing along the boundary layer upstream of the separation. At the separation, *i.e.* $x/\delta_i = 37.1$, the pressure fluctuates intermittently in the interaction zone, with a pic varying between a lower mean value p_1 in the region ahead of the separation and a higher value p_2 in the separated region as observed by Kistler *et al* .[15] The mean pressure at the point of interest follows:

$$\gamma p = \gamma\, p_2 + (1-\gamma)\, p_1 \tag{1}$$

where γ is the intermittent factor.
The mean-square fluctuation p'^2 around the wall mean pressure can be predicted using Kistler's equation from:[15]

$$p'^2 = \underbrace{\gamma(1-\gamma)\,(p_2-p_1)^2}_{\text{low frequency part}} + \underbrace{\overbrace{\gamma\, p_2'^2}^{\text{shear layer}} + \overbrace{(1-\gamma)\, p_1'^2}^{\text{boundary layer}}}_{\text{high frequency part}} \tag{2}$$

Kistler's function is plotted along with the present computation. The result indicates that the theoretical function perfectly matches the computed wall distribution within the interaction zone.

Fig. 4-a shows the separation location x_s for both wall-resolved and wall-modeled simulations. This location is detected where the near-wall velocity becomes negative; $\overline{u}_w(x_s(t),t) < 0$ with $\overline{u}_w$ is the θ-averaged streamwise velocity at the first near-wall point. Fig. 4-b shows the normalized spectrum of the separation location, where two energetic peaks can be identified. The tone at a Strouhal number ($S_t = f.\delta_i/u_{i,\infty}$) of $S_t = 0.0067$ is the most energetic one and can be assimilated to the resonant tone illustrated by Zaman *et al* [27] who proposed the following correlation to compute it:

$$f_r = \frac{c_0^2 - u_e^2}{4\, c_0\, L_{s,e}}, \tag{3}$$

with u_e and c_0 are the averaged velocity at the nozzle exit and the corresponding speed of sound, respectively. $L_{s,e}$ is the length between the mean separation location and the nozzle exit. Eq. 3 can be used for the present investigation as it fits the requirements proposed by Zaman (mild opening angle of divergent, low Reynolds number, subsonic Mach jet). The predicted Strouhal number of resonance can be computed by:

$$St = \frac{1 - M_e^2}{M_e}\,\frac{\delta_i}{4L_{s,e}}, \tag{4}$$

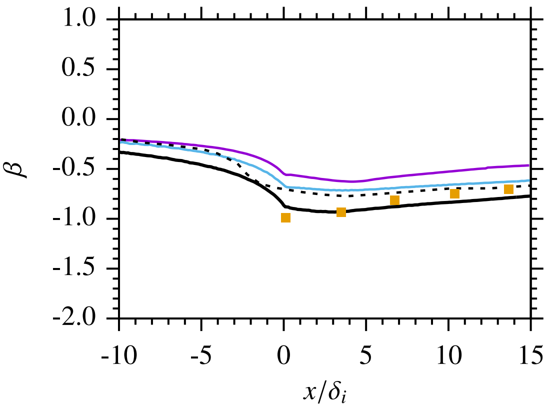

Figure 2: Longitudinal distribution of the normalized pressure gradient; —: planar wall-resolved LES from,[20] - : planar wall-resolved LES from,[18] —: cylindrical wall-resolved LES from,[20] —: cylindrical WM-LES, ■: planar experimental results from.[14]

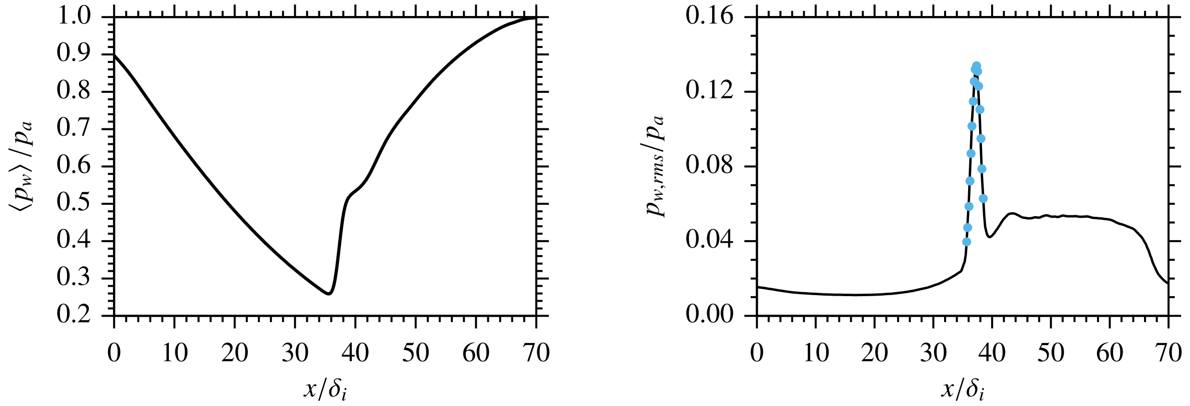

(a)

(b)

Figure 3: Longitudinal distribution of the normalized; (a) mean wall pressure, (b) r.m.s pressure —: present LES , ●: Kistler's function (Eq. 2).

where M_e is the averaged Mach number at the nozzle exit.

The computed Strouhal number of resonance is about 0.007 which is close to the peak of energy observed in Fig. 4-b. The strong coupling between the separation region and the nozzle exit seems to fit one-quarter wavelength as observed in the planar nozzle flow.[20] A second peak can be observed around Strouhal number of 0.015 is due to the recirculating bubbles at the separated zone upstream of the nozzle exit (shown later). Above $St = 0.015$, the spectrum drops and no energy can be seen in the high-frequency range.

3.1 Side-loads analysis

The streamwise force (F_x) and the side-loads (wall-normal F_y and spanwise F_z forces) are computed as:

$$\vec{F} = \int_S (p_w - p_a) \cdot \vec{n} \, \mathrm{d}s, \tag{5}$$

where p_w is the wall pressure, p_a the ambiant pressure, ds the local surface element where the force apply, $\vec{n}_i$ the normal vector to the surface and S the total surface of the nozzle. The forces are integrated along the azimuthal direction θ from the inlet to the nozzle exit. Table 2 shows averaged and r.m.s forces in each direction. The side-loads, *i.e.* y- and z-direction forces can be combined to form a resultant vector force ($F_{\vec{n}}$).

$$F_{\vec{n}} = \sqrt{F_y^2 + F_z^2}, \tag{6}$$

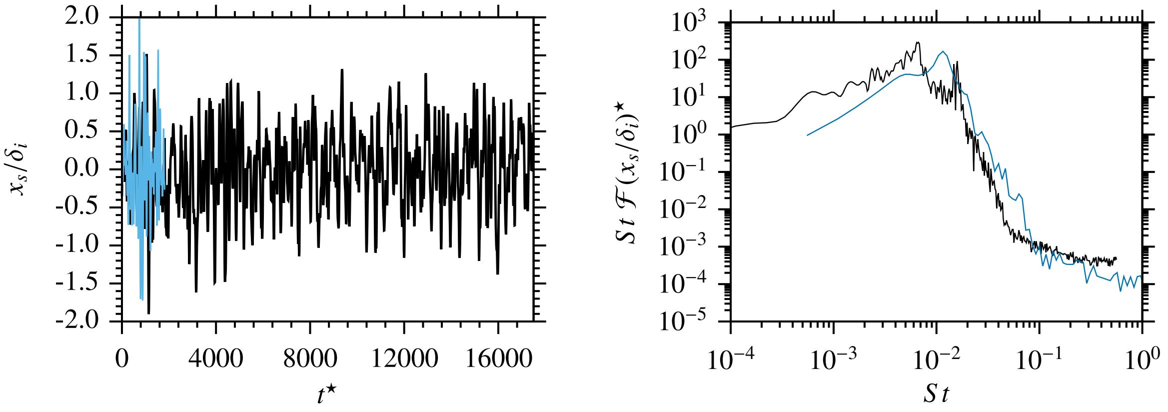

(a) (b)

Figure 4: (a) Time variation of the separation location; —: WM-LES, —: WR-LES from.[20] (b) Normalized premultiplied spectrum of the separation location for; —: WM-LES, —: WR-LES from.[20]

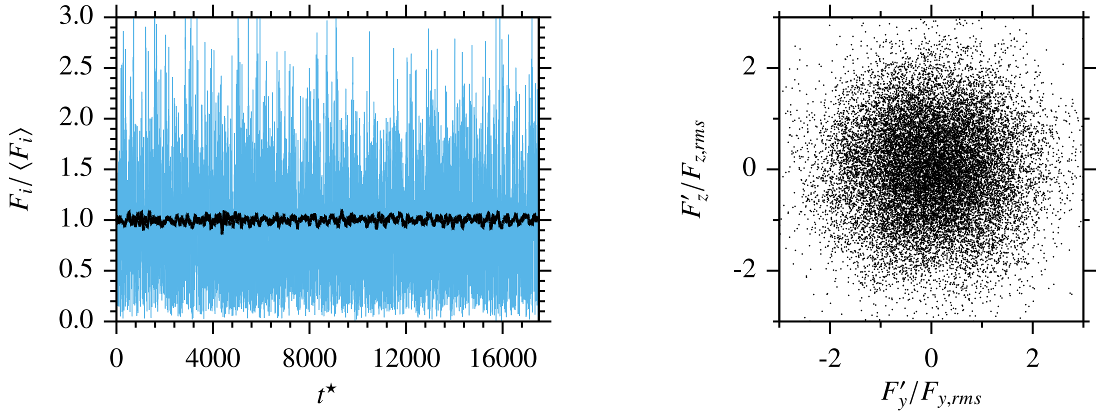

(a) (b)

Figure 5: (a) Time evolution of the forces in the; —: streamwise direction F_x, —: wall-normal direction $F_{\vec{n}}$. (b) WM-LES: Polar plot of the two-component fluctuating normalized side-loads.

The angle (Θ_F) between F_y and F_z is given by:

$$\Theta_F = \tan^{-1}\left(\frac{F_z}{F_y}\right). \tag{7}$$

Fig. 5-a shows the streamwise force and the side-loads as function of time. One can notice that the fluctuations of the streamwise force are weaker compared to the side-loads. The mild nozzle opening angle and the small fluctuations of the separation line result in a weaker r.m.s of the streamwise force. Fig. 5-b shows a typical polar plot of the side-loads. One can notice the isotropic and random behavior of the fluctuating side-loads. Both y- and z-direction forces are uncorrelated. They follow a two-dimensional Gaussian distribution with equal variance with a zero mean value which fits the Rayleigh distribution:

$$f(\eta,\sigma) = \frac{\eta}{\sigma^2}\exp\left(-\eta^2/(2\,\sigma^2)\right), \tag{8}$$

η is a random value of the side-loads amplitude and σ the r.m.s of the amplitude.
The computed side-loads probability density function is shown in Fig. 8, and compared to both experimental results and URANS computations from Deck *et al* .[5] The present LES indicates that the distribution of the side-loads amplitude follows a Rayleigh distribution as proposed by many authors.[5,24] The scale parameter $\sigma \sim 0.8862$ fits reasonably the prediction of the Rayleigh distribution function ($< 0.1\%$) where the URANS computations was about 2%. These correlations shows that the two components of side-loads are not correlated. Thus, the side-loads do not have any twirling movement and the angle of the force is acting randomly on the structure of the nozzle.

Fig. 6 and 7 show the normalized spectrum of the streamwise force and the side-loads, respectively. The normal-

Case	$\langle F_x \rangle / F_{isen}$	$\langle F_{\vec{n}} \rangle / F_{isen}$	$F_{x,rms}/F_{isen}$	$F_{y,rms}$	$F_{z,rms}/F_{isen}$
WM-LES	50 %	84 %	1.4 %	67 %	67 %

Table 2: Averaged and r.m.s nozzle forces scaled by the isentropic normal force $\vec{F}_{isn} = \int_S (p_{isn} - p_a) \cdot \vec{n}\, \mathrm{d}s$.

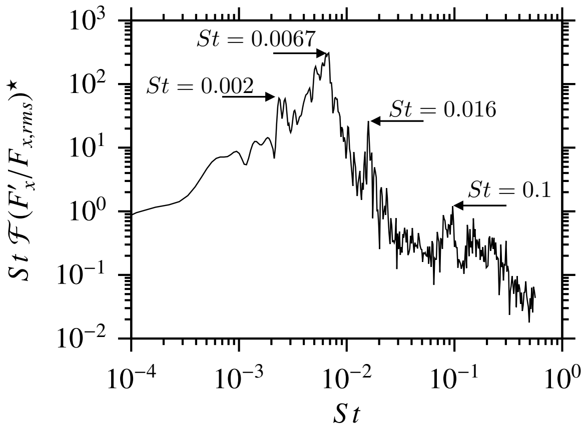

Figure 6: Normalized pre-multiplied spectrum of the fluctuating streamwise force $F'_x/F_{x,rms}$.

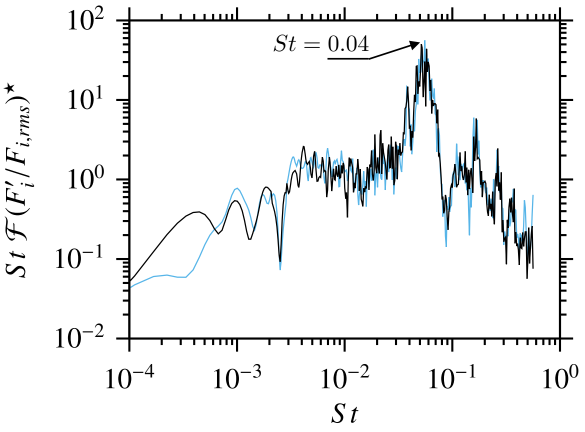

Figure 7: Normalized pre-multiplied spectra of the fluctuating side-loads; —:$F'_y/F_{y,rms}$, —:$F'_z/F_{z,rms}$.

ized spectrum $St\,\mathcal{F}(\phi)^*$ as a function of ϕ is computed as:

$$St\mathcal{F}(\phi)^* = \frac{St\mathcal{F}(\phi)}{\int_{St} St\mathcal{F}(\phi) dSt}. \tag{9}$$

As observed in the planar case,[20] the streamwise force is sensitive to the low-frequency oscillations while the side-loads seem to be receptive to the higher frequency ranges. The same peaks observed in Fig. 4b are captured in the streamwise force spectrum. The main tone computed by the spectrum is about $St = 0.0067$, similarly to the previous analysis of the separation location. The second peak at $St = 0.016$ is also captured within the streamwise force. Another peak of energy is observed in the high-frequency range at $St = 0.1$. As observed in the planar nozzle[20] and following the literature review,[7,25] the fluctuations of about a tenth of the Strouhal number can be originated from the mixing layer downstream of the separation.

The side-load spectrum is plotted in Fig. 7. Similarly to the planar nozzle flow,[20] the side-loads are affected by the high-frequency range oscillations arising from the separated flow downstream of the shock. The two side-loads components ($F_y^{'}$ and $F_z^{'}$) have similar spectrum abroad the frequency range of the spectrum. The main peak for both is around $St = 4 \times 10^{-2}$. When using the Strouhal number based on the nozzle exit conditions defined as $St_D = \varepsilon D_e/(\delta_i M_e) St$, whith ε, D_e, δ_i and M_e are the nozzle area ratio, the exit diameter, the boundary layer thickness at the inlet and the Mach number at the exit, respectively, the main peak is found at $St_D \simeq 1$. According to the previous studies,[4] the nozzle lip is known to generate trailing-edge noises at $St_D = 1$. These noises affect the exit pressure field which generates acoustic waves upstream through the subsonic recirculation area. Changing the nozzle lip curvature or reducing the flange width could lead to a shifted range of frequencies as observed by Ponton *et al* .[23]

Based on the side-load spectra, one can identify different peaks. For this purpose, full time-resolved wall probes, covering a wide range of frequencies ($10^{-4} \leq St \leq 1$) are used. Fig. 9 shows the spectra of the normalized fluctuating wall pressure field for different x-locations. One can notice that the energy is centered around $St = 1$ in the throat region. At the separation region, the peak captured at $St = 6.7 \times 10^{-3}$ is similar to the peak observed in the separation spectrum (Fig. 4). The resonant tone is also captured at the nozzle exit along with the recirculation bubble $St = 1.6 \times 10^{-2}$ and with the trailing-edge noises at $St = 4 \times 10^{-2}$.

Fig. 10 shows the frequency analysis using the centerline slice. For each point in the x-y plane, the Strouhal number associated with the maximum energy from the normalized pressure field spectrum is displayed using iso-contours values of the different captured phenomena. A color map is associated with each phenomenon. Hence for:

- $St = 0.0067$, the resonant tone predicted by Zaman *et al* [27] is captured close to the λ-shock and in the second shock train at $x/\delta_i \sim 50$. It is interesting to notice that the second shock oscillates at the same resonant tone as the first λ-shock (Fig. 11).

DOI: 10.13009/EUCASS2019-140

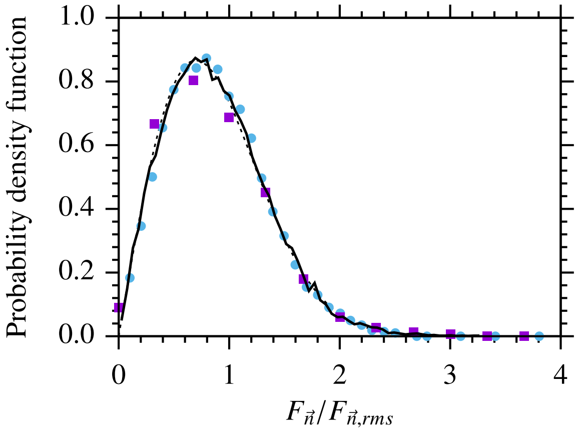

Figure 8: Probability density function of the side-loads $F_{\vec{n}}$; —: current LES, - - : Rayleigh distribution, •: experiment from Deck *et al* ,[5] ■: URANS from Deck *et al* .[5]

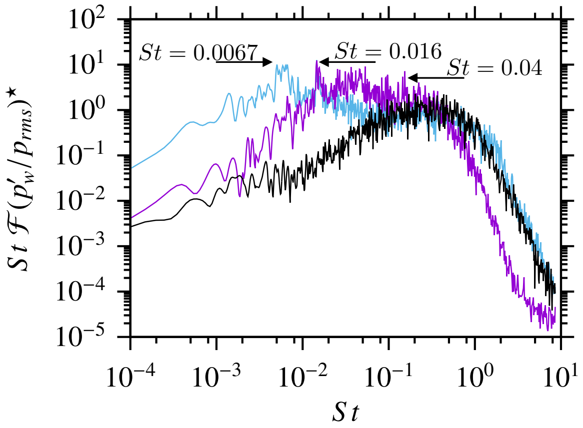

Figure 9: Normalized pre-multiplied spectra of the fluctuating pressure field at the wall; —: in the incoming boundary layer $x/\delta_i = 0$, —: at the separation $x/\delta_i \sim 37.1$, —: at the exit $x/\delta_i = 66$.

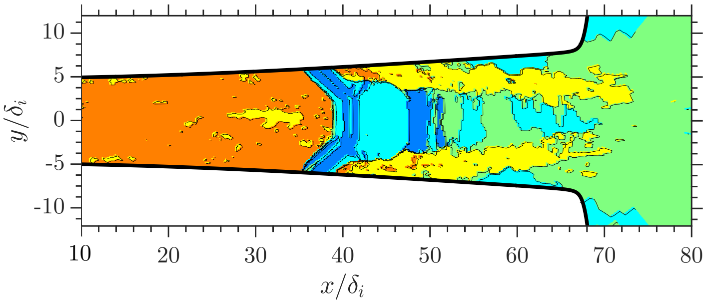

Figure 10: Frequency analysis in the x-y plane showing the Strouhal number associated with the most dominant frequencies extracted from the normalized pressure field spectra $St\,\mathcal{F}(p'/p_{rms})$; Orange zone ($St \sim 1$): boundary layer turbulence, yellow zone (downstream of the shock) ($St \sim 0.1$): mixing layer unsteadiness, (upstream of the shock): inlet profile unsteadiness, green zone ($St \sim 0.04$): trailing-edge noises, cyan zone ($St \sim 0.016$): recirculation bubbles and blue zone ($St \sim 0.0067$): resonant tone.

- $St = 0.016$, the subsonic flow downstream of the separation, at $x/\delta_i \sim 60$, is trapped between the mixing layer and the wall producing small unsteady eddies oscillating at this specific frequency. This phenomenon strongly affects the lateral forces.
- $St = 0.04$, the trailing-edge noises from the lip is captured at the nozzle exit and in the atmospheric region. The frequency at which the noise is seen is similar to the vortex shedding phenomenon taking place in the external nozzle jet.
- $St = 0.1$, the mixing layer developing from the separation region is observed at this frequency. The large two-dimensional Kelvin-Helmholtz vortices impact the exit conditions, modifying thereby effective exit area and the position of the separation shock.
- $St = 1$, upstream of the separation, the pressure fluctuations are dominant in the range of the turbulent boundary layer frequencies (fig.11). The shock position is slightly correlated with the upstream condition. However, the asymmetry of the separation is strongly influenced by the incoming boundary-layer turbulence, particularly observed in the planar nozzle.

3.2 Effect of the nozzle divergent half-angle

The effects of increasing the nozzle divergent half-angle is investigated. As already pointed out by Hunter,[13] the opening of the divergent section causes an upstream displacement of the shock and the associated boundary layer separation. In this part, we kept the same geometry of the nozzle while increasing the angle of the divergent to 7°, which gives a surface ratio of $\varepsilon = 2.6$ compared to $\varepsilon = 1.6$ for $\alpha_1 = 3°$.

DOI: 10.13009/EUCASS2019-140

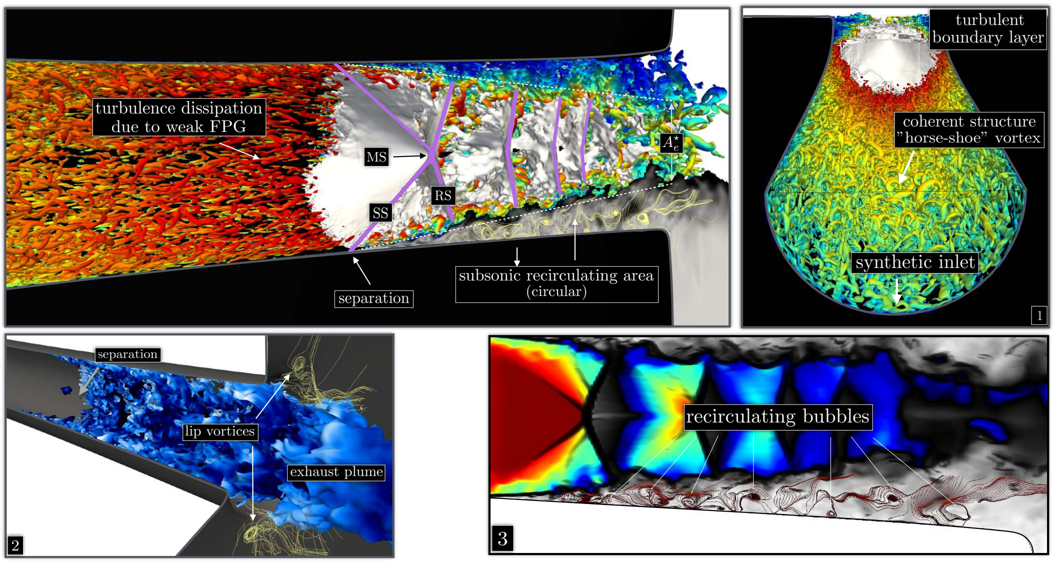

Figure 11: Iso-contour of Q criterion colored by the velocity field (blue: slow, red: fast); MS: Mach stem, SS: separated shock, RS: reflected shock, $A_e^\star$: effective exit area; grayscale surface: Numerical schlieren picture at $\theta = 0$, white volume: iso-volume of the velocity gradient $\nabla||u||$.

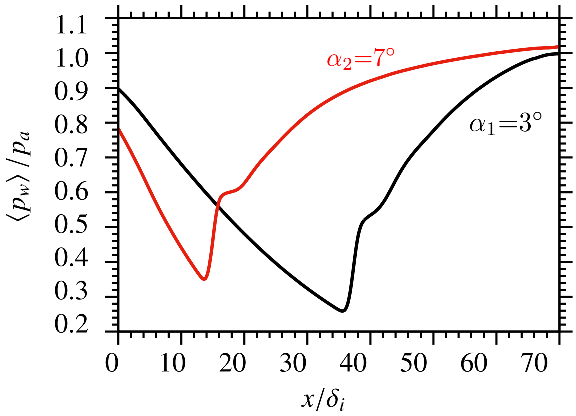

Figure 12: Normalized wall pressure distribution along x-direction.

In Fig. 12, the separation point is shifted backward by $22\delta_i$ approximately which represents a large displacement compared to the small change of the angle. However, the shock oscillations keep the same amplitude as the original case over a distance of $d = 2\delta_i$. The effect of changing the divergent angle on the wall loads are presented in Fig. 13. Fig. 13-a shows the energy spectrum of the streamwise forces for both geometries. The two spectra are very similar with almost the same energy peaks apart from the fact that are a little off for the second geometry. This is mainly due to the shock position as already reported by Zaman *et al* .[27] Fig. 13-b shows the energy spectrum of the side-loads. One can notice that the phenomena responsible for the lateral charges are independent of the position of the shock.

To better understand the energetic peaks presented in both Fig. 13-a and Fig. 13-b, spectra-maps are plotted to identify the spatial distribution of the energetic zones for different modes. As mentioned before, Fig. 14-a and Fig. 14-b show that the modes with $St = 0.0028$ and $St = 0.0045$ correspond to the shock oscillations. Fig. 14-c shows clear evidence of the existence of some energetic eddies trapped between the mixing layer and the nozzle wall with a characteristic frequency of $St = 0.016$. Finally, the high-frequency modes corresponding to $St = 0.8 - 1.0$ come mainly from the upstream boundary layer with a small part coming from the mixing layer, Fig. 14-d.

DOI: 10.13009/EUCASS2019-140

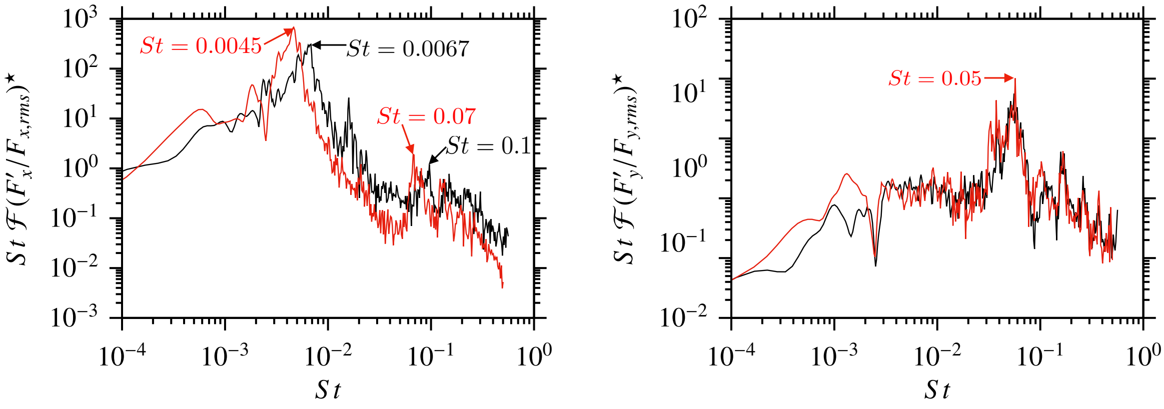

(a) (b)

Figure 13: Normalized pre-multiplied spectrum of: (a) the fluctuating streamwise force $F'_x/F_{x,rms}$, (b) the fluctuating side-loads; —:$F'_y/F_{y,rms}$, —:$\alpha_1 = 3°$, —: $\alpha_2 = 7°$.

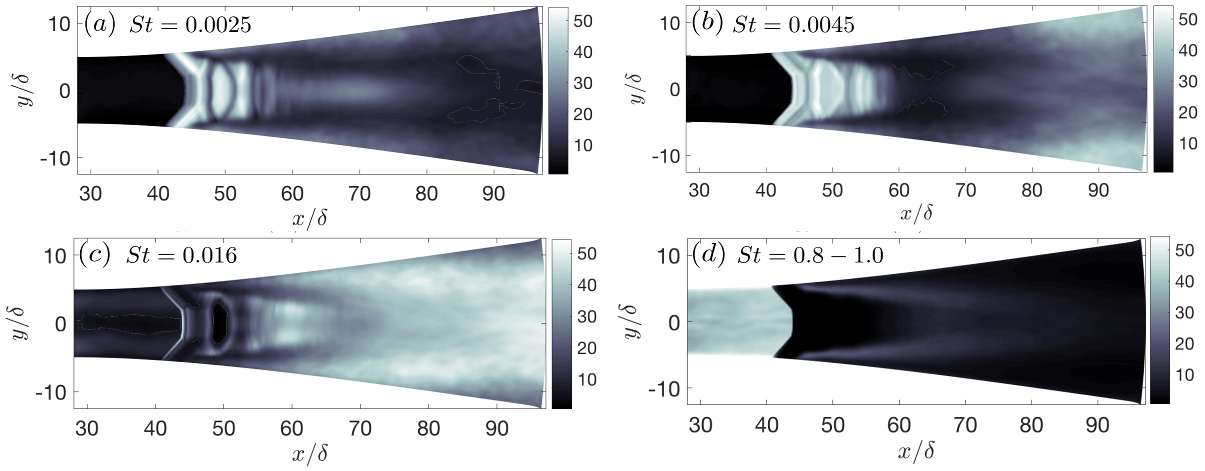

Figure 14: Spectral frequency distribution in the x-y plane showing the energy rate associated with the most dominant frequencies extracted from the normalized pressure field spectra $St\,\mathcal{F}(p'/p_{rms})$.

DOI: 10.13009/EUCASS2019-140

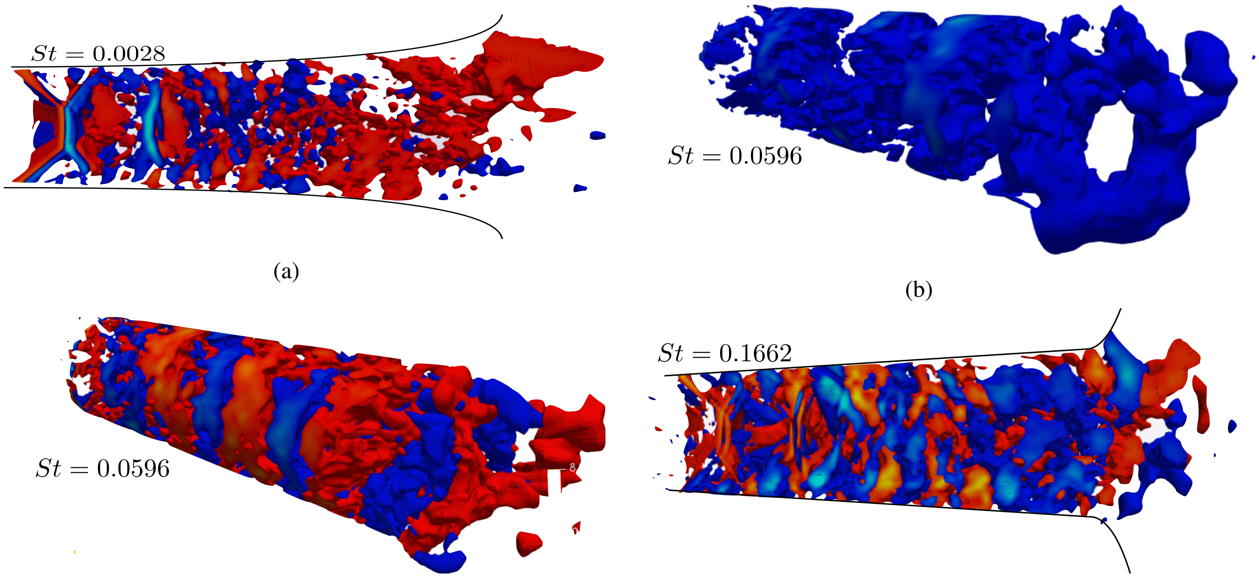

(a) (b) (c) (d)

Figure 15: Isovolume of the real part with negative and positive pressure fluctuations. Red to yellow color indicates positive pressure fluctuations, yellow being the highest. Dark to light blue indicates negative pressure fluctuations, light blue being the lowest.

3.3 Dynamic Mode Decomposition (DMD) analysis

The DMD is applied to the LES data to better understand the space organisation of the energetic modes observed in the previous spectral analysis. Given the wide scale of the frequencies present in this flow (Fig. 6 and Fig. 7) and in order to focus on the low frequencies, a Multi-resolution DMD (MrDMD), developed by Kutz *et al* ,[16] is used, in which the signal is splited into a hierarchy of multi-resolution time-scale components.

A first look at the shape of the modes indicates the existence of two type of modes; non-helical and helical modes. As a result, the observed modes can be classified into three categories:

- $St \in [..., 0.0168]$: corresponding to the flopping modes which are, at the origin of the streamwise forces through the oscillatory movement of different shock structures.

- $St \in]0.0168, 0.1000]$: associated with helical mode. They represent vortical structures of different sizes that become finer when increasing the frequency. These structures appear very close to the nozzle wall downstream of the shocked region, this leads to consider those modes as the major responsible for the side-loads.

- $St \in [0.1000, 0.5000]$: corresponding to the oscillations at high energy vortical structures originated from the mixing layer. These modes manifest close to the nozzle axis and they have less influence on the spectrum of side-loads.

4. Conclusion

In this paper, wall-modeled large-eddy simulations of supersonic conical nozzles have been presented. The results showed that the amplitude of the separation line is less important in the cylindrical nozzle compared to the planar one because of the increased pressure gradient upstream of the throat, resulting from the reduced cross-section. Spectral analysis shows the existence of low-frequency phenomena resulting mainly from the shock system oscillations. It is found that the side-loads are affected by the high-frequency range oscillations arising from the separated flow downstream of the shock. The DMD analysis highlights the existence of two types of modes; the non-helical (flopping) which is low frequency appearing mainly in the spectra of the streamwise forces and the helical mode which is dominated by high frequency oscillations and appears essentially in the spectra of the side-loads.

DOI: 10.13009/EUCASS2019-140

5. Acknowledgments

This work was performed using high-performance computing (HPC) resources from GENCI (Grand Equipement National de Calcul Scientific) [grant 0211640] and from CRIANN (*Centre Régional Informatique et d'Applications Numériques de Normandie*), Rouen, France, [grant 1998022].

References

[1] O. H. Ünalmis and D. S. Dolling. Decay of wall pressure field and structure of a mach 5 adiabatic turbulent boundary layer. AIAA Paper, 94:23–63, 1994.

[2] S. J. Beresh, N. T. Clemens, and D. S. Dolling. Relationship between upstream turbulent boundary-layer velocity fluctuations and separation shock unsteadiness. *AIAA J.*, 40(12):2412–2422, 2002.

[3] A. Bourgoing and P Reijasse. Experimental analysis of unsteady separated flows in a supersonic planar nozzle. *Shock Waves*, 14(4):251–258, 2005.

[4] S Bühler, L Kleiser, and C Bogey. Simulation of subsonic turbulent nozzle jet flow and its near-field sound. *AIAA J.*, 52(8):1653–1669, 2014.

[5] S Deck and A T Nguyen. Unsteady side loads in a thrust-optimized contour nozzle at hysteresis regime. *AIAA J.*, 42(9):1878–1888, 2004.

[6] P Dupont, C Haddad, J P Ardissone, and J F Debiéve. Space and time organisation of a shock wave/turbulent boundary layer interaction. *Aerospace Science & Technology*, 9(7):561 – 572, 2005.

[7] P Dupont, C Haddad, and J F Debiève. Space and time organization in a shock-induced separated boundary layer. *J. Fluid Mech.*, 559:255–277, 2006.

[8] J P Dussauge, P Dupont, and J F Debiève. Unsteadiness in shock wave boundary layer interaction with separation. *Aerospace Science & Technology*, 10:85–91, 2006.

[9] B Ganapathisubramani, N T Clemens, and D S Dolling. Effects of upstream boundary layer on the unsteadiness of shock-induced separation. *J. Fluid Mech.*, 585:369–394, 2007.

[10] A Hadjadj and M Onofri. Nozzle flow separation. *Shock Waves*, 19(3):163–169, Jul 2009.

[11] A Hadjadj, Y Perrot, and S Verma. Numerical study of shock/boundary layer interaction in supersonic overexpanded nozzles. *Aerospace Science & Technology*, 42:158 – 168, 2015.

[12] G Hagemann, M Frey, and W Koschel. Appearance of restricted shock separation in rocket nozzles. *J. Propulsion & Power*, 18(3):577–584, 2002.

[13] C. A. Hunter. Experimental investigation of separated nozzle flows. *J. Propulsion & Power*, 20(3):527–532, 2004.

[14] A D Johnson and D Papamoschou. Instability of shock-induced nozzle flow separation. *Phys Fluids*, 22(1):16102, 2010.

[15] A L Kistler. Fluctuating wall pressure under a separated supersonic flow. *J. Acoustical Society of America*, 36(3):543–550, 1964.

[16] J Kutz, X Fu, and S Brunton. Multiresolution dynamic mode decomposition. *SIAM J. Applied Dynamical Systems*, 15(2):713–735, 2016.

[17] E Martelli, P P Ciottoli, L Saccoccio, F Nasuti, M Valorani, and M Bernardini. Characterization of unsteadiness in an overexpanded planar nozzle. *AIAA J.*, 57(1):239–251, 2019.

[18] B Olson and S Lele. Large-eddy simulation of an over-expanded planar nozzle. *41st AIAA Fluid Dynamics Conference and Exhibit*, 2010.

[19] S Piponniau, J P Dussauge, J F Debieve, and P Dupont. A simple model for low-frequency unsteadiness in shock-induced separation. *J. Fluid Mech.*, 629:87–108, 2009.

DOI: 10.13009/EUCASS2019-140

[20] A Piquet. *Physical analysis and numerical simulation of the separation phenomenon in over-expanded nozzle flow*. PhD thesis, Normandie Université, 2017.

[21] A Piquet, B Zebiri, A Hadjadj, and M S Shadloo. A parallel high-order compressible flows solver with domain decomposition method in the generalized curvilinear coordinates system. *Int. J. Numerical Methods Heat & Fluid Flow*, 2019.

[22] S Pirozzoli and F Grasso. Direct numerical simulation of impinging shock wave/turbulent boundary layer interaction at $M = 2.25$. *Phys Fluids*, 18(6):065113, 2006.

[23] M K Ponton and J M Seiner. The effects of nozzle exit lip thickness on plume resonance. *J. Sound & Vibration*, 154(3):531–549, 1992.

[24] M Terhardt, G Hagemann, and M Frey. Flow separation and side-load behavior of truncated ideal rocket nozzles. *AIAA Paper*, 3686:2001, 2001.

[25] E Touber and N D Sandham. Large-eddy simulation of low-frequency unsteadiness in a turbulent shock-induced separation bubble. *Theoretical & Computational Fluid Dynamics*, 23:79–107, 2009.

[26] S Verma, M Chidambaranathan, and A Hadjadj. Analysis of shock unsteadiness in a supersonic over-expanded planar nozzle. *European J. Mech. - B/Fluids*, 68:55 – 65, 2018.

[27] K B Zaman, M Dahl, T Bencic, and C Loh. Investigation of a transonic resonance with convergent–divergent nozzles. *J. Fluid Mech.*, 463:313–343, 2002.